RSC Advances

PAPER

View Article Online
View Journal | View Issue

Cite this: *RSC Adv.*, 2025, **15**, 47366

Upgrading the therapeutic potential of catechin against Ehrlich carcinoma and mitigating oxidative stress in the liver employing chitosan polyaspartate as nanodelivery vehicles

Mohammad Y. Alfaifi,[ab] Mustafa R. Abdulbaqi,[c] Wesam Abd El-Fattah,[d] Ali A. Shati,[ab] Serag Eldin I. Elbehairi,[ab] Reda F. M. Elshaarawy,[ef] Waleed M. Serag[*e] and Yasser A. Hassan[gh]

This study aims to design and develop new chitosan polyaspartate nanovehicles (CPANVs) to enhance the targeting delivery and bioavailability of catechin (CAT). Thus, augmenting its anticancer efficacy against Ehrlich ascites carcinoma (EAC) in the peritoneal cavities of Swiss albino mice and without impairing the liver or its functions. Initially, CAT@CPANVs were synthesized through double emulsification followed by ionotropic gelation processes, and the physicochemical and morphological characteristics of this nanoformulation were investigated. Thereafter, the *in vivo* studies were performed on four equally divided groups of sixty Swiss albino female mice: control (G1), drug group (G2, CAT@CPANVs-treated), positive control (G3, EAC-bearing), and therapeutic (G4, EACs plus CAT@CPANVs). Noteworthy, EAC-bearing mice treated with CAT@CPANVs showed reduced levels of S100A14, Angptl-2, AST, ALT, cholesterol, LDL-cholesterol, triglyceride, MDA, TNF-α, and caspase 3 and elevated levels of GSH, CAT, superoxide dismutase (SOD), albumin, total protein, and Bcl2. These findings indicate that CPANVs exhibit chemotherapeutic and chemopreventive actions with remarkable capabilities to reduce the viability and volume of EACs. Additionally, biochemical, immunohistochemical, and histological investigations showed that CAT@CPANVs can enhance liver tissue by maintaining redox balance and minimizing oxidative stress.

Received 18th August 2025
Accepted 9th November 2025

DOI: 10.1039/d5ra06086a

rsc.li/rsc-advances

1. Introduction

Ehrlich ascites carcinoma cells (EACs) are widely used to simulate cancer effects on host health. Studies show EACs cause significant health impacts in mice, including renal toxicity and DNA damage, shown by elevated urea and creatinine levels and oxidative stress. Intraperitoneal EAC injection causes rapid cancer cell proliferation, leading to ascites tumors and systemic effects like liver inflammation.[1] Notably, EACs have been linked to an imbalance in redox state and lower levels of antioxidant enzymes, highlighting the oxidative stress caused by these cells.[2]

Catechin (CAT), a polyphenolic flavonoid that occurs naturally in many plants, has attracted enormous interest in recent years because of its multiple very valuable biological properties.[3] Among these properties, the antioxidant, anti-inflammatory, and antimicrobial capabilities of catechin make it a really interesting compound for potential use in the prevention and treatment of a host of different kinds of diseases, chiefly cancer, but also cardiovascular disorders and neurodegenerative conditions like Alzheimer's disease.[4,5] Because of its great therapeutic potential, scientists are very interested in figuring out how to use catechin more successfully for various kinds of medicinal treatments. However, the biomedical utility of catechin is hampered by very poor bioavailability and poor pharmacokinetics, meaning that catechin is not very soluble in water and is not very stable in solution.[6] Nonetheless, several strategies have been attempted to boost the bioavailability and medicinal effectiveness of catechin including nanoencapsulation, forming complexes with other substances, and modifying catechin's structure.[7] Investigating

[a]*Central Labs, King Khalid University, Alqura'a, P. O. Box 960, Abha, Saudia Arabia*
[b]*King Khalid University, Faculty of Science, Biology Department, Abha 9004, Saudi Arabia*
[c]*Department of pharmaceutics, College of Pharmacy, Al-Naji University, Baghdad, Iraq*
[d]*Department of Chemistry, College of Science, Imam Mohammad Ibn Saud Islamic University (IMSIU), P. O. Box 5701, Riyadh 11432, Saudi Arabia*
[e]*Department of Chemistry, Faculty of Science, Suez University, 43533 Suez, Egypt. E-mail: waleed.ibrahim@suezuniv.edu.eg*
[f]*Institut für Anorganische Chemie und Strukturchemie, Heinrich-Heine Universität Düsseldorf, Düsseldorf, Germany*
[g]*Department of pharmaceutics, College of Pharmacy, Al-Kitab University, Kirkuk 36015, Iraq*
[h]*Department of Pharmaceutics and Pharmaceutical Technology, Faculty of Pharmacy, Delta University for Science and Technology, Gamasa, Egypt*

opportunities to broaden catechin bioavailability and improve therapeutic efficacy could help researchers tap into the biomedical potential of these compounds, pushing transformative, catechin-based therapeutics closer to the clinic.

The emerging field of nanomedicine has turned to explore many nanoparticulate systems for targeted and efficient drug delivery.[8] Among them, chitosan–polyaspartate nanoparticles (CPANPs) have received considerable attention for their potential to enhance the therapeutic efficacy and safety profile of various biomedical applications, due to their biocompatibility and biodegradability, as well as their ability to be made functionally diverse.[9] Chitosan was chosen to make new nanocarriers for a number of important reasons, such as being biocompatible and biodegradable, which means they are not very toxic. The most useful thing about it is that it has a positive charge, which makes the nanocarriers stick strongly to negatively charged cancer cells and mucosal tissues. This gives the catechin inside more time to be absorbed. Also, because it is cationic, it can easily form complexes with polyanionic polymers like polyaspartate. This creates a strong polyelectrolyte complex that keeps the drug from breaking down too soon and allows for a controlled, long-lasting release profile.[10] The advantages of CPANPs include their ability to encapsulate a wide range of therapeutic agents, protect them from degradation, and facilitate targeted delivery to specific sites within the body, thereby reducing systemic side effects and improving patient outcomes.[9] Furthermore, the mucoadhesive properties of chitosan enable these nanoparticles to adhere to mucosal surfaces, prolonging the residence time of the delivered therapeutic agents and enhancing their absorption. Despite these advantages, there exist opportunities for enhancement, particularly in terms of optimizing the nanoparticles' stability, scalability, and targeting specificity. For example, 5-fluorouracil (5-Fu) was nanoencapsulated with CPANPs, leading to a substantial improvement in the medicine's ability to affect carcinoid tumors in nude mice.[11] In another study, CPANPs were synthesized using ionotropic gelation technique to create a vehicle suitable for the encapsulation of hydrophilic drugs, with the objective of targeting the effective treatment of tuberculosis.[12] A recent study investigated the development of tea polyphenol-loaded CPANPs (TP@CPANPs) incorporated into polyvinyl alcohol (PVA) nanofibers to enhance the shelf life of fruits. This packaging system offers a viable approach for the intelligent regulation of active substance release for food preservation.[13] As research continues to elucidate the properties and potential applications of CPANPs, these versatile delivery systems hold significant promise for advancing the field of nanomedicine and improving human health outcomes.

Considering these noteworthy facts, the current study aimed to improve CAT's stability, bioavailability, pharmacokinetics, and pharmacodynamics by encasing it in chitosan polyaspartate nanodelivery vehicles (CPANVs) to fabricate CAT@CPANVs. By encapsulating CAT within CPANVs, this study leverages benefits of both components. The novelty lies in using CPANVs, which enhance catechin's solubility and stability while potentially synergizing its anticancer activity through targeted delivery and sustained release, augmenting cytotoxic effects against EACs and mitigating oxidative stress in the liver.

2. Material and methods

2.1. Chemicals and instrumentations

Specifications for these chemical and instrumentations used in this work were provided in the SI.

2.2. Preparation of CAT-loaded CPANVs

The CAT-loaded CPANVs (CAT@CPANVs) were synthesized using a modified version of the previously adapted methods,[14,15] with a slight modification. Briefly, 10 mL of an aqueous 2.0 mg mL^{-1} CAT solution (prepared in DI water) was combined with 20 mL of the pre-prepared PAA solution (2.0 mg mL^{-1}) under vigorous magnetic stirring. Subsequently, the CAT/PAA mixture was incrementally introduced into the LMC solution (6.0 mg mL^{-1}, 25 mL) while maintaining vigorous magnetic stirring at 25 °C and pH 6.0, until the formation of dense turbidity, indicating the formation of CAT@CPANVs. The self-assembled nanoparticles were continuously stirred for an extra 30 min. After centrifuging the CAT@CPANVs at 13 000 rpm for 15 min at room temperature, the loaded nanovehicles were washed three times with phosphate buffer and then with MQW to eliminate any unincorporated CAT. The CAT@CPANVs were subsequently re-dispersed in 10 mL of DIW and ultrasonicated for 5 min in an ice bath to achieve a uniform dispersion. This dispersion was then freeze-dried over 72 hours, and the resulting CAT@CPANVs were stored at −18 °C.

2.3. Entrapment efficiency and loading capacity of CAT in CAT@CPANVs

The CAT@CPANVs' entrapment efficiency (EE) and loading capacity (LC) was determined by sonicating a 5 mg sample of the nanovehicles with 1 mL of ethanol for one minute, followed by centrifugation at 13 000 rpm. A UV-visible spectrophotometer set at 425 nm[16] was used to estimate the free CAT after the supernatant was collected and kept at 4 °C. A series of standard ethanolic CAT solutions of serial concentrations between 200 and 1000 μg mL^{-1} were used in order create a standard curve. The following formula (eqn (1)) and (eqn (2)) were employed to express the EE:

$$\mathrm{EE\%} = \frac{\text{amount of CAT in supernatant}}{\text{initial amount of CAT}} \times 100 \quad (1)$$

$$\mathrm{LC\%} = \frac{\text{total CAT} - \text{CAT in supernatant}}{\text{mass}_{\text{CPANVs}}} \times 100 \quad (2)$$

2.4. *In vitro* release kinetics

The dialysis method was applied to study the *in vitro* release of CAT from CAT@CPANVs using a dialysis method as described in the SI. The cumulative CAT release from CAT@CPANVs was calculated employing formula (eqn (3)):

$$\mathrm{OR}\% = \sum_{t=0}^{t} \frac{\text{released CAT amount}}{\text{original CAT amount}} \times 100 \quad (3)$$

After that, numerous kinetic models, such as zero order, first-order, second-order, Higuchi, and Korsmeyer–Peppas equations, were used to examine the *in vitro* release results.[17]

2.5. *In vivo* studies

Comprehensive details regarding these studies, including animal sampling and grouping, tumor sampling, response dose curve, experimental design, LD_{50} and EACs viability determination, and life span, are provided in the SI.

2.6. Biochemical investigation

2.6.1. Apoptotic and fibrotic markers. S100A14 and angiopoietin-like protein 2 (Angptl2) levels in serum were estimated using solid-phase sandwich ELISA (Glory Science Co., Ltd, USA).

2.6.2. Liver functions test. The colorimetric diagnostic kit methods Abcam (USA) were to used determine albumin,[18] total protein,[19] aspartate aminotransferase (AST), and alanine aminotransferase (ALT) levels in serum samples.[20]

2.6.3. Lipid profile test. The lipid profile parameters including total cholesterol,[21] LDL, VLDL and HDL,[22] as well as triglyceride[23] were estimated in serum using the colorimetric diagnostic kit methods Abcam (USA).

2.6.4. Antioxidants. The activities of antioxidant enzymes, reduced (GSH),[24] catalase (Cat),[25] and superoxide dismutase (SOD)[26] were measured calorimetrically in liver tissues using manufacturer's procedure (BioVision, Inc. USA).

2.6.5. Lipid peroxide. The malondialdehyde (MAD) level was measured in liver tissues by colorimetric assay (BioVision, Inc. USA).[27]

2.6.6. Detection of caspase-3 and Bcl2. The levels of caspase-3 and Bcl2 were evaluated by solid-phase sandwich ELISA in liver tissues (Abcam, USA).

2.7. Immunohistochemical investigations

TNF-α was detected immunohistochemically using liver blocks. Sections were treated with 0.3% H_2O_2 in PBS and 10% goat serum in PBST for 30 min each. They were then treated with rabbit anti-TNF-α (Leader in Biomolecular Solutions for Life Science). A semi-quantitative study of immunohistochemical staining and protein expression, using the Histo-score approach, calculated the proportion and degree of positive cells. To get the H-score, we multiply fractions by scores and sum them.

2.8. Histopathologic examination

According to Layton *et al.*,[28] for microscopic analysis, the liver tissues of every rat were removed and kept for a day in 10% neutral buffered formalin. After being dehydrated in progressively higher alcohol concentrations, they underwent xylene refinement and paraffin immobilization. Hematoxylin-Eosin (H&E) was used to stain the paraffin blocks after they had been cut into 5 μm tissue slices. A light microscope (Olympus BX53, Japan) was used to study the morphological changes in the liver tissues.

2.9. Estimation of apoptosis

Apoptotic cell death in liver tissues was quantitatively assessed using an eBioscience Annexin V-FITC/Propidium Iodide (PI) apoptosis detection kit (Thermo Fisher Scientific) in accordance with the manufacturer's instructions. Fresh liver tissue was used to create cell suspensions. After cell collection, the cells were washed twice for ten minutes at 4 °C using 100 μL of PBS. Next, 100 μL of binding buffer and 5 μL of Annexin V-FITC were added to each well. After 10 minutes of incubation at room temperature, 400 μL of PBS was added. Prior to inspection, the cells were stained with PI. To ascertain the level of apoptosis, the stained cells were analyzed by flow cytometry (BD FACS-Canto II, BD Biosciences, USA) within an hour of staining.

2.10. Statistical analysis

We used SPSS for Windows v 26.0 (Armonk, NY: IBM Corp.) for data analysis. Data normality was examined using Shapiro–Wilk test. Descriptive data were expressed as means ± SDs. Groups were compared using unidirectional ANOVAs with *post hoc* Bonferroni Tests for pairwise comparisons. Significance was evaluated at $P < 0.05$.

3. Result and discussion

3.1. Synthesis protocol

The self-assembly process for the synthesis of catechin-loaded chitosan–polyaspartate nanovehicles (CAT@CPANVs) is outlined in Scheme 1. Low molecular weight chitosan (LMC) and poly-L-aspartic acid (PAA) are the two key components of the core–shell nanostructure. Nanovehicles are formed mainly through spontaneous assembly driven by complementary electrostatic interactions between the positively charged amine groups ($-NH_3^+$) of chitosan and the negatively charged carboxylate groups (CCO^-) of PAA, forming a stable polyelectrolyte complex. The assembled supramolecules create a three-dimensional nanoscale framework that features effective binding sites, such as the carboxylate groups of polyaspartate and the hydroxyl and amine groups of chitosan, for encapsulating drugs.

CAT, a polyphenolic flavonoid with multiple hydroxyl groups, is incorporated into the nanovehicle network through a combination of H-bonding and electrostatic interactions. The structure of catechin is rich in hydroxyl groups, which allow for extensive H-bonding with two components of the nanovehicle, chitosan and PAA. These form strong H-bonds with catechin because they have carbonyl, amine, and other functionalities that hydrogen bond very well with hydroxyl groups. In addition, CAT has ionizable phenolic groups that can engage in electrostatic interactions with the positively charged amine groups ($-NH_3^+$) of chitosan. This stabilizing interaction occurs because the energetics of such an interaction is favorable for both catechin and the polymer.

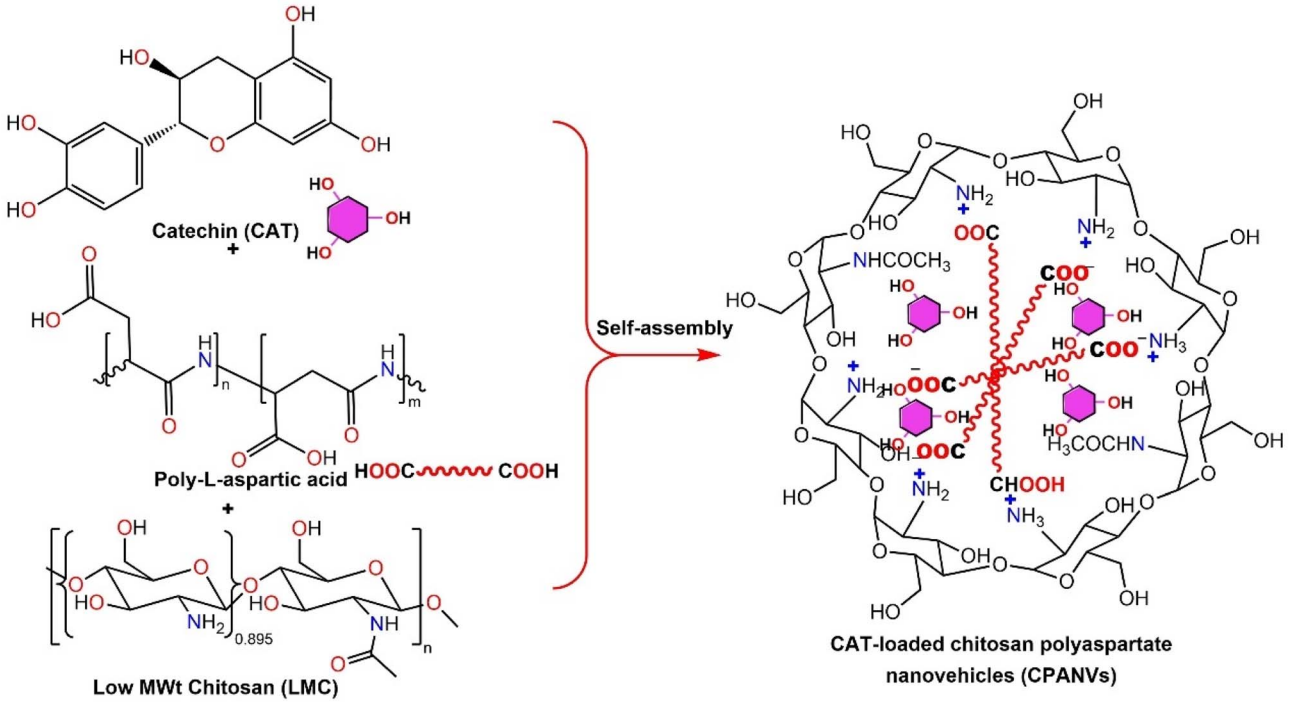

Scheme 1 Schematic illustration for the preparation of CAT-loaded chitosan–polyaspartate nanovehicles (CAT@CPANVs).

3.2. Physicochemical and morphological characterization

3.2.1. FTIR. The FTIR spectra CAT-loaded chitosan–polyaspartate nanovehicles (CAT@CPANVs) and their nascent precursors are presented in Fig. 1A. The spectra clarify the molecular interactions that occur during the formation of the nanovehicle and its subsequent loading of CAT. LMC's spectrum shows broad and intense absorption centered at 3360 cm^{-1}, attributed to overlapping O–H and N–H stretching vibrations. Peaks near 2900 cm^{-1} (C–H stretching), 1652 cm^{-1} (amide I: C=O stretching), 1570 cm^{-1} (N–H bending), and 1070 cm^{-1} (C–O–C stretching) are also seen. These peaks are characteristic of the chitosan's backbone.[29] Conversely, the PAA spectrum shows prominent bands at 3430 cm^{-1}, which correspond to the stretching vibrations of N–H and O–H bonds, and within the region of 1712–1651 cm^{-1}, which are associated with the carbonyl stretching vibrations of the carboxylic acid and amide I groups. Moreover, bands at 1589 and 1400 cm^{-1} could be designated as the asymmetric and symmetric stretching vibrations of the carboxylate group.[30]

When LMC and PAA are physically mixed, slight spectral shifts and broadenings are noticed, especially for the stretches that occur around the spectral regions associated with the carboxyl and hydroxyl groups. These shifts and broadening effects suggest that the interaction between LMC and PAA is not just a simple mixing of two components. Rather, these are interactions involve the formation of hydrogen bonds and some ionic interactions.[31] On contrast, the spectrum of CPANVs shows more pronounced changes, which include the broadening and shifting of the O–H/N–H stretching band, and a decrease in the intensity of the COO^- bands. The spectrum of CPANVs reveals more pronounced changes, broadening and shifting the O–H/N–H stretching band, and the COO^- bands show decreased intensity. These changes indicate that the ionic interactions of CPANVs are stronger than that of LMC and PAA in the solution state and that the amino groups of LMC and the carboxyl groups of PAA may forming amide bonds, thus confirming that the amino and carboxyl groups serve as the basic building blocks for the self-assembly of CPANVs.[32] This assembly was driven by complementary electrostatic and H-bonding interactions. Once CAT is encapsulated, *i.e.*, CAT@CPANVs, the spectrum exhibits a bunch of additional features that comes from the polyphenolic structure of CAT. More specifically, the characteristic CAT peaks that were observed at 1620 cm^{-1} and 1513 cm^{-1}, corresponding to aromatic C=C skeletal vibrations of the flavonoid ring system.[33] Additionally, there are a slight shift and broadening of the band associated with hydroxyl group vibration, as in the 3400 cm^{-1} region, which implies that there might be some H-bonding between CAT and the polymeric matrix.[34] Pure CAT shows sharp absorption bands in the range of 1256–1117 cm^{-1}, which correspond to C–O stretching in phenolic and alcoholic groups. But in the spectrum of CAT@CPANVs, these same bands appear to be broadened and dampened, suggesting that there are some kind of molecular interactions going on between the CAT and the CPANVs at the "nanocarrier" level.

3.3. Zeta potential and particle size distribution

Fig. 1B presents the zeta potential (ZP) histogram of CAT@CPANVs, revealing a sharp, monomodal distribution centered at approximately +35.12 mV. This positive charge boosts

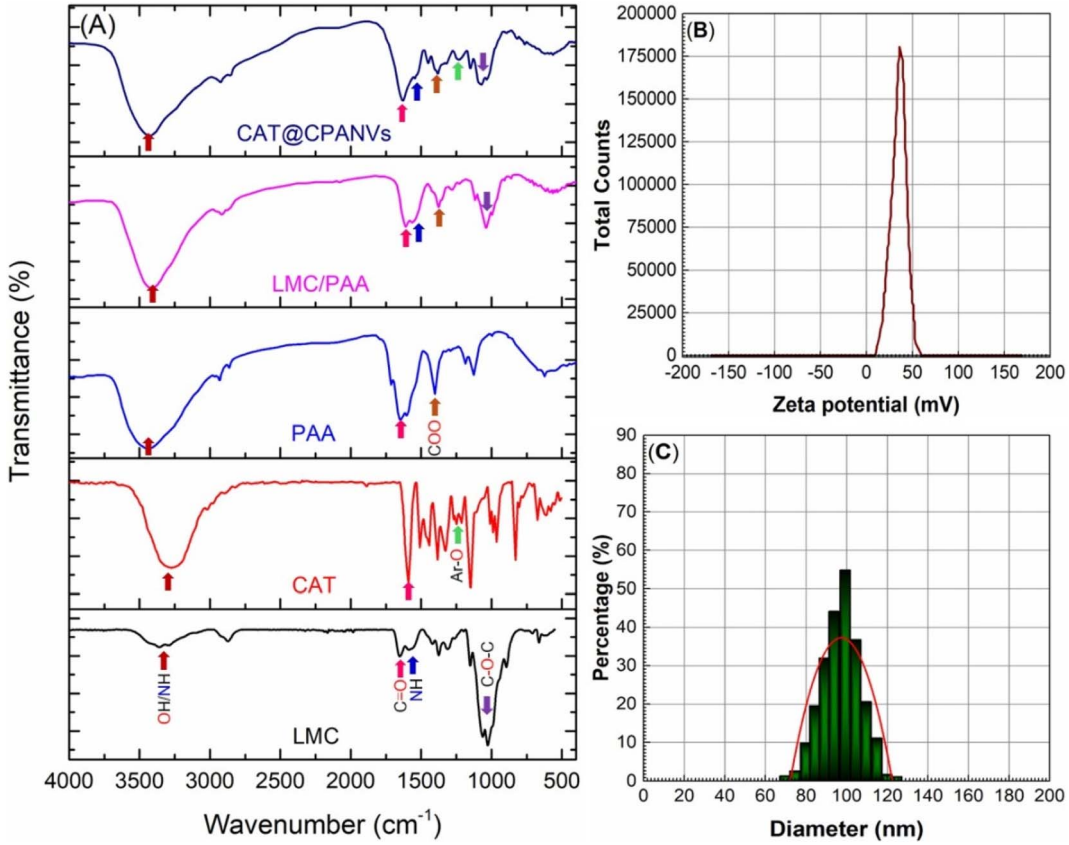

Fig. 1 (A) FTIR spectra of CAT-loaded chitosan polyaspartate nanovehicles (CAT@CPANVs) and their precursors: low molecular weight chitosan (LMC), catechin (CAT), polyaspartic acid (PAA), and LMC/PAA physical mixture. (B) Zeta potential (ZP) and (C) particle size distribution (PSD) histograms of CAT@CPANVs.

mucoadhesion and interaction with cellular membranes that carry a negative charge. A zeta potential with a magnitude greater than 30 mV (*i.e.*, a value more positive than +30 mV or more negative than −30 mV) is generally considered indicative of sufficient electrostatic repulsion to ensure good colloidal stability, which is essential for guaranteeing the long-term dispersion stability of the system in aqueous media.[35–37] The high ZP value and its narrow range indicate that the CAT@CPANVs possess outstanding colloidal stability, which is attributed to strong electrostatic repulsion that prevents the particles from agglomeration. Interestingly, the ZP of the new nanoformulation levels out all previously reported CAT-loaded chitosan-based nanoformulations, which exhibit ZPs ranging between +24.0 and +33.5 mV.[14,33,38]

On the other hand, the particle size distribution (PSD) of CAT@CPANVs (Fig. 1C) reveals a narrow and monomodal distribution of nanoparticles. Most of the particles fall within the 70–120 nm range, with an average hydrodynamic diameter (HDD) of 95.86 ± 11.89 nm and a polydispersity index of 0.31 ± 0.02. This indicates that they possess a well-defined size, characteristic of nanovehicles. This size range is beneficial for pharmaceutical applications because NPs of sizes <200 nm displayed an enhanced permeability and retention effect in tumor tissues. They also show improved cellular uptake through mechanisms of endocytosis.[39] Furthermore, the narrow distribution indicates high reproducibility and minimal polydispersity in our formulations; both factors are important for consistent biological performance and regulatory compliance.

3.4. Morphological characteristics

The CAT@CPANVs' surface morphology and its nanoscale architecture were investigated using scanning electron microscopy (SEM, Fig. 2A) and transmission electron microscopy (TEM, Fig. 2B). The SEM image shows moderately rough and textured surface resulting from the aggregation of the primary nanovehicles during the drying process, which is a good indication of successful formation of nanoparticles and anchoring of CAT molecules within the chitosan–polyaspartate matrix. With possible ramifications for mechanical characteristics and drug retention within the structure, these structures imply that the nanovehicles are not only porous but also capable of adequately stabilizing the trapped CAT molecules within the polymeric matrix.[40] Notable, the clustering, observed in the new nanovehicles, is typical of chitosan-based nanosystems due to interparticle interactions and matrix cohesion.[41,42]

TEM offers even more detailed investigation into the internal structure and dimensions of nanovehicles. They are spherical particles with well-defined, sharp boundaries are clearly visible and show a narrow size distribution, with diameters that are

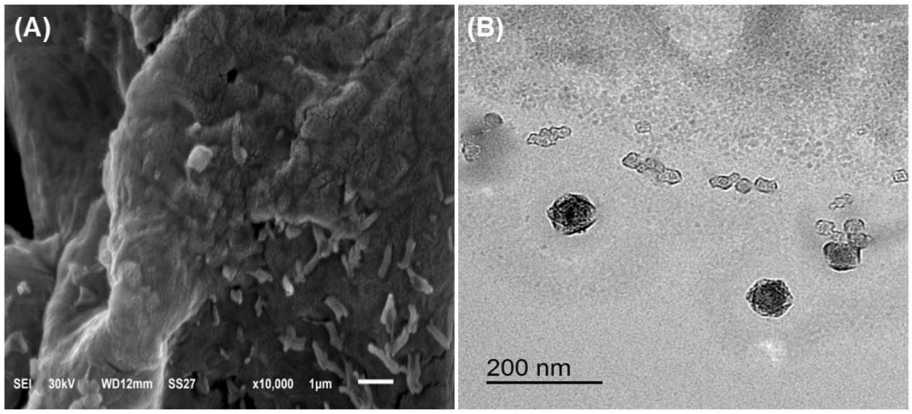

Fig. 2 (A) SEM microimage and (B) TEM nanoimage of CAT@CPANVs.

mainly in the range of 35–89 nm. This range is lower than that obtained from the DLS measurements (70–120 nm) and supports the appearance of monodisperse nanoparticles. Several aspects of nanoparticle characterization can be responsible for the discrepancy between the CAT@CPANV particle sizes determined by DLS measurements and TEM imaging. TEM makes it possible to directly view dried nanoparticles, enabling previously unheard-of accuracy in size and shape measurements. In contrast, DLS is used to measure the hydrodynamic diameter of a variety of suspended particles, including the particle itself and the hydration layer. Because of this, the larger size DLS measurement can somewhat be accounted for by the hydration layer, in addition to potential aggregation, or the swelling of the particle in an aqueous environment.[43] Furthermore, the polydispersity of the sample can also contribute to this discrepancy. DLS is far more sensitive to the larger particles present in the system; therefore, it skews the size distribution towards larger values. Significantly, the TEM micrograph showed no signs of aggregation or fusion, serving to bolster the already confirmed strong electrostatic stabilization implied by the high positive zeta potential.

3.5. Storage stability of TPs#CDCS

The stability of CAT@CPANVs during short-term storage was investigated by analyzing its principle physicochemical properties including particle size and PDI over a period of 1 week. Mimicking physiological environment former was maintained at room temperature (25 °C) in PBS buffer pH (7.4). Fig. S1 (SI) indicates the physical stability during storage of the nanoformulation. The average HD did not change, remaining around 95.89 nm for the study group on day 0 and being about 105.47 nm on day 7 (small, statistically non-significant difference). This value of PDI was low, which implied a uniform distribution of particle size and free from large aggregation and damage. This physical stability stems from the high positive zeta potential of the nanocarriers, imparting strong electrostatic repulsion between particles, which is a critical attribute for formulation in nanomedicine. These results indicate that CAT@CPANVs nanoformulation is a physiochemically stable.

3.6. Encapsulation efficiency and loading capacity

The amphiphilic characteristics of the formulation, combined with the PAA–chitosan structure, resulted in substantial drug entrapment, as demonstrated by the loading capacity of CAT by CPANVs and the encapsulation efficiency of 85.26 ± 7.79% and 15.56 ± 0.9%, respectively. CPANVs enhance encapsulation through electrostatic interactions and restrict drug diffusion, while the PAA core provides a hydrophilic environment conducive to CAT encapsulation. The crosslinking of PAA strengthens the network, thereby reducing drug diffusion both during and after formation.[44] Overall, the high EE and LC achieved support the CPANVs platform's capacity as an efficient nanocarrier for catechin and other pharmacological agents.

3.7. Release kinetics

The release behavior of CAT from CAT@CPANVs was studied at pH 7.4 and 5.5 at 37 °C for 24 h. As shown in Fig. 3A, release was faster and more extensive at pH 5.5 compared to pH 7.4. An initial burst release occurred within 2 h at both pH values, with 55% CAT released at pH 5.5 and 45% at pH 7.4, likely from CAT near the surface or loosely bound in the chitosan shell. After this burst, release slowed, controlled by CAT diffusion through the chitosan–PAA matrix. A sustained release continued for 24 hours, reaching ~84% at pH 5.5 and ~75% at pH 7.4.

The enhanced release under acidic conditions occurs through protonation of chitosan's amino groups, increasing swelling and polymer dissolution for faster drug diffusion. This pH-responsive behavior suits tumor-targeted delivery, where environments are more acidic than normal tissues, aligning with previous chitosan nanocarrier studies. Wu *et al.* documented pH-sensitive CAT release from chitosan–TPP nanoparticles, showing higher release at pH 6.5 compared to pH 7.4.[45] Tang *et al.* showed that catechin in chitosan-poly(γ-glutamic acid) (γ-PGA) nanocarriers exhibited greater release in acidic media, enhancing intracellular availability in cancer cells.[14] The controlled release ensures prolonged CAT availability, improving efficacy and reducing dosing frequency. The release at physiological pH limits drug leakage during circulation, enhancing the nanocarrier's stability and targeting.

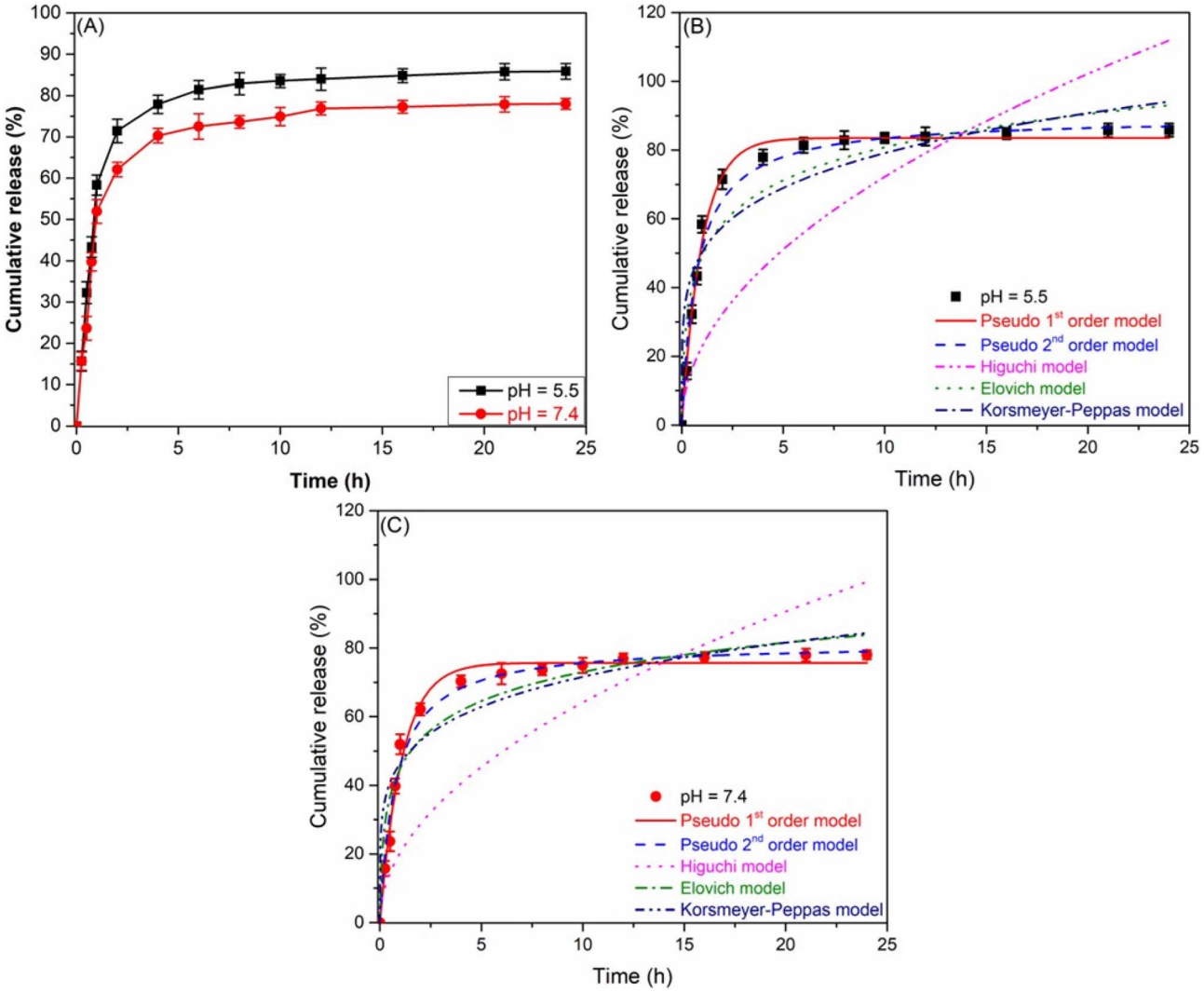

Fig. 3 (A) *In vitro* cumulative release profile of catechin (CAT) from CAT@CPANVs at 37 °C, over 24 h under simulated physiological (pH 7.4) and mildly acidic (pH 5.5) conditions. (B and C) Kinetic model fitting parameters for the *in vitro* release of CAT from CAT@CPANVs under different pH conditions.

To elucidate CAT release from CAT@CPANVs, data were analyzed using five models: pseudo-first order, pseudo-second order, Higuchi, Elovich, and Korsmeyer–Peppas, at pH 7.4 and 5.5, to identify the best model (Fig. 3 B and C), Table 1). The pseudo-first order model showed the best fit, with $R^2 = 0.9981$ at pH 5.5 and $R^2 = 0.9973$ at pH 7.4, suggesting CAT release is primarily concentration-dependent and diffusion-controlled. The pseudo-second order model also showed strong fit ($R^2 = 0.99149$ at pH 5.5 and 0.995579 at pH 7.4), indicating CAT-matrix interactions may play a secondary role. The Korsmeyer–Peppas model showed moderate fit ($R^2 =$ 0.9671 at pH 5.5 and 0.9646 at pH 7.4), with diffusion exponent values below 0.45 ($n = 0.1976$ and 0.1878), indicating Fickian diffusion as the primary release mechanism.[46] Although the Elovich model also provided a good fit with R^2 values around 0.98, it was slightly less effective than the first-order model, implying that its use is more suitable for the initial stages of desorption. Overall, the release kinetics of CAT from CAT@CPANVs are best described by the pseudo-first order model, supported by Fickian diffusion mechanisms, with pH-dependent acceleration under acidic conditions.

3.8. Effects of CAT@CPANVs on mice

3.8.1. Median LD_{50}. To assess its acute toxicity, CAT@CPANVs was injected intrapertonially to determine its median LD_{50}. There were no harmful effects at any concentrations (1–100 mg kg^{-1}) employed. Thus, CAT@CPANVs treatment is safe up to 100 mg kg^{-1}.

3.8.2. Lifespan prolongation. The administration of CAT@CPANVs to mice resulted in a significant increase in the therapeutic group's life span, with a 38.89% extension compared to the positive control group, thereby demonstrating the efficacy of CAT@CPANVs treatment in prolonging the average lifespan of the animals.

Table 1 Kinetic model fitting parameters for the *in vitro* release of CAT from CAT@CPANVs under different pH conditions

Model	Parameter	pH = 5.5	pH = 7.4
Pseudo-first order	CR (%)	83.52263	75.67774
	k_1 (min^{-1})	1.00798	0.91836
	R^2	0.99811	0.99733
Pseudo-second order	CR (%)	89.60265	81.4859
	k_2 (g mg^{-1} min^{-1})	0.01505	0.015839
	R^2	0.99149	0.995579
Higuchi	K_h (mg g^{-1})	22.83968	20.27375
	R^2	0.83029	0.80369
Elovich	α (g mg^{-1} min^{-1})	452.54889	456.27845
	β (mg g^{-1})	0.07155	0.06546
	R^2	0.98007	0.080988
Korsmeyer–Peppas	K_{kp} (g mg^{-1} min^{-1})	50.2127	46.46746
	n	0.1976	0.18777
	R^2	0.9671	0.96461

3.9. Impacts of CAT@CPANVs on EAC

3.9.1. Dose–response CuCate. Ehrlich carcinoma was clearly suppressed in a dose-dependent manner by CAT@CPANVs in Swiss albino mice, as illustrated in Fig. 4A. The dose–response cuCate showed a non-linear pattern. CAT@CPANVs achieved maximum tumor suppression at a dose of 15 mg kg^{-1}, where the EAC cell count declined dramatically to nearly 40 × 10^6 cells. Doses below this level (2.5–10 mg kg^{-1}) produced the curious effect of enhancing tumor proliferation, while a dose of 20 mg kg^{-1} again showed paradoxical effects and appeared to be too much in terms of CAT's tumor-promoting (or at least not inhibiting) effects. The most direct interpretation of these results is that CAT has a very precise range of effective doses and would have to be given with a great deal of precision to achieve any tumor-tracking (or at least tumor-holding) effects.

3.9.2. Impact on the number of EAC and quantity. In Fig. 3B, the group receiving 15 mg kg^{-1} of CAT@CPANVs

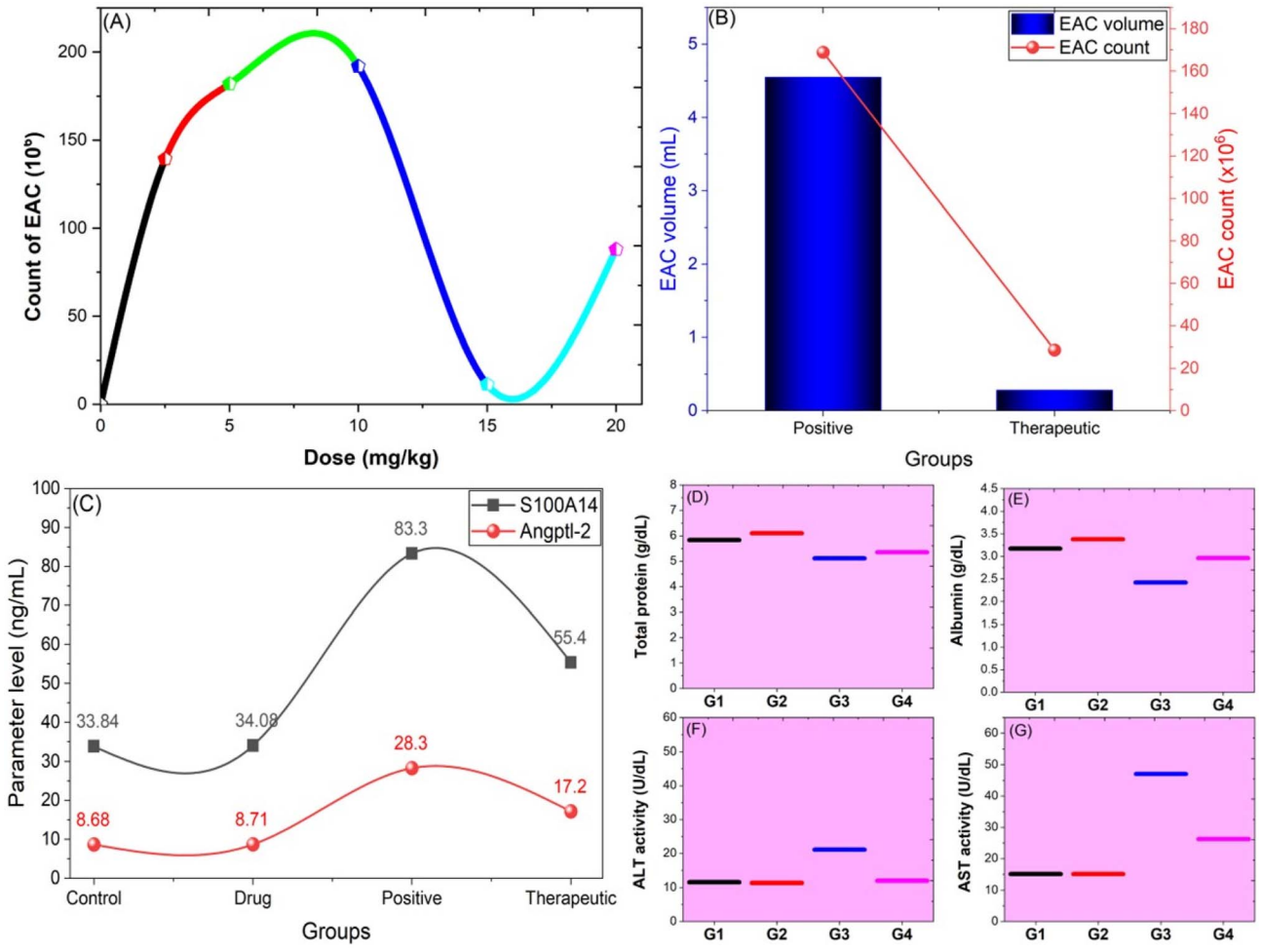

Fig. 4 Therapeutic impacts of CAT@CPANVs on the (A) EAC cell count (dose–response cuCate), (B) Ehrlich volume and EAC cell count, (C) levels of pro-apoptotic/fibrotic markers (S100A14 (ng ml^{-1}) and Angptl-2 (ng ml^{-1})), (D) total protein (g dl^{-1}), (E) conc. of albumin (g dl^{-1}), (F) activity of serum alanine aminotransferase (U dl^{-1}), and (G) activity of serum aspartate aminotransferase (U dl^{-1}). G1 (control) was given 10 days of intraperitoneal injection (IPJ) of normal saline; G2 (drug group) received IP administration of CAT@CPANVs (15 mg kg^{-1}) daily for 10 days. G3 (EAC-positive group) was administered EACs (2.5 ×10^6 cells/mice) by IPJ on the initial day; G4 (therapeutic group) CAT@CPANVs were given IP at 15 mg kg^{-1} daily for 10 days after EAC injection.

showed a remarkable decrease in both the average EAC volume and the number of viable cells, in contrast to the positive group with untreated tumors. Notably, the positive group had an average EAC volume of 4.55 ± 0.58 mL, as shown in Fig. 4B, while in the therapeutic group, it fell by −93.85% to 0.28 ± 0.14 mL ($p < 0.05$). In the EAC group, the average number of EACs was 168.83 ± 6.98 (10^6) cells. However, as shown in Fig. 4B, this number fell by 83.02% to 28.67 ± 12.54 (10^6) cells. These findings demonstrate the exceptional anti-tumor effectiveness of CAT when administered through PAA–chitosan nanovehicles, likely due to enhanced bioavailability, increased cellular uptake, and targeted action at the tumor site.

3.9.3. S100A14 level. High doses of S100A14 cause ROS generation and apoptosis. Thus, exogenous S100A14 triggers apoptosis or cell growth at different doses through RAGE ligation.[47] S100A14 is higher in liver fibrosis patients than healthy individuals and increases as disease progresses.[48] S100A14 increases p53, which prevents cell division.[49]

S100A14 levels showed significant differences between study groups. Group (G3) had the highest mean value (83.3 ± 0.41), followed by group (G4) with 55.4 ± 0.13), while groups (G2) and (G1) had the lowest values (34.08 ± 0.23) and (33.84 ± 0.51), respectively. Compared to control, percentage change was higher in the positive group (147%), therapeutic group (64%) and marginally higher in the drug group (0.7%) (Fig. 4C). These findings align with previous reports showing S100A14 is expressed in human cancers and regulates biological processes like apoptosis and proliferation.[50] S100A14 was found to trigger cell proliferation and metastasis by activating the MAPK pathway.[51]

3.9.4. Angiopoietin-like protein 2 (Angptl2) level. Angptl2 increases inflammatory cytokines, macrophage infiltration in adipose tissue, and vascular inflammation in transgenic mice.[52] Increased adipose tissue and circulatory inflammation, associated with Angptl2, play a significant role in NAFLD pathophysiology.[53] According to Tian *et al.*,[54] Angptl2 stimulates angiogenesis, oxidative stress, apoptosis, inflammation, and fibrotic remodelling. There are significant differences between groups in Angptl2 levels. The positive group (G3) showed highest values (28.3 ± 0.22), followed by G4 (17.2 ± 0.13) and drug G2 group (8.71 ± 0.23). The control group (G1) had lowest values (8.68 ± 0.32). Compared to control, changes were higher in positive group by 226%, therapeutic group (98%) and drug group (0.35%) (Fig. 4C). These findings are consistent with the previous results show that the serum Angptl2 level accurately differentiates between patients with malignancies and healthy controls, and relates to tumour progression.[55]

3.10. Liver function tests

3.10.1. Impact of CAT@CPANVs on total protein. Total protein testing aids liver problem diagnosis by measuring liver function. Total plasma protein production can be affected by illnesses, while liver dysfunction often shows reduced TSP levels.[56] Total protein and albumin values in EACs groups are significantly lower ($p < 0.001$) than drug and negative control groups, as shown in Fig. 4. The G4 group exhibits greater significance compared to the EACs group. Our findings showed a significant difference ($F = 68.43$, $P < 0.001$) in total protein content between groups. The drug-treated group (G2) recorded the highest value of 6.1 ± 0.08, followed by G1 with 5.83 ± 0.11, and G4 with 5.35 ± 0.14. EAC group (G3) had 5.11 ± 0.08. Drug group showed a 27.1% rise, while positive control and therapeutic groups decreased by −7.8% and −3.3% compared with control (Fig. 4D). Between the EACs group and the treated mice group, there was no discernible difference in the serum total protein concentration.[57]

3.10.2. Impact of CAT@CPANVs on the albumin. Regarding albumin, variations existed between groups ($F = 79.82$, $P < 0.001$). The disparities between groups were substantial. Group 2 had the highest mean value (3.38 ± 0.03), followed by (G1) group (3.17 ± 0.02) and (G4) group (2.96 ± 0.05), while (G3) group had the smallest amount (2.42 ± 0.05). The positive group fell by −29.5% compared with control, the therapeutic group increased by 23.6%, while the drug group decreased by 7.1% (Fig. 4E). The EAC bearing positive control group showed a considerable decrease in serum albumin.[57]

3.10.3. Impact of CAT@CPANVs on aminotransferase. The most biochemical parameters commonly used for hepatic injury are AST and ALT.[58] Hepatic injury such as liver necrosis and inflammation may be the cause of the EAC-bearing mice's high elevation in ALT and AST activity.

3.10.4. Impact of CAT@CPANVs on ALT activity. Regarding the ALT activity with control, there is significant difference between groups under study ($F = 60.97$, $P < 0.001$). With the positive group (G3), the high mean value was noted (21.12 ± 1.11) followed therapeutic group (G4) (11.95 ± 0.3) and control group (G1) (11.53 ± 0.18) while drug group (G2) had the lowest value (11.34 ± 0.32). By contrast to the control, the drug group saw a reduction of −1.67%, but the positive group (81.20%) and therapeutic groups (6.93%) showed an increase in percentage change (Fig. 4F).

3.10.5. Impact of CAT@CPANVs on AST activity. The study groups differ significantly from one another in terms of the AST activity ($F = 553.49$, $P < 0.001$). The (G3) group's high mean level (47.1 ± 0.33) then in (G4) group (26.2 ± 0.55). The (G2) group (15.11 ± 0.18) and the (G1) group had smallest amount (15.08 ± 0.03). In contrast to the control, the percentage change was significantly higher in the therapeutic group (73.44%) and positive group (212.42%), but only slightly higher in the drug group (0.16%) (Fig. 4G). These results are consistent with a prior study,[59] which shows that there is a highly significant difference between the serum activities of ALT and AST in the mice in the EACs group and the control group. These results corroborate earlier studies[60] that indicated significant increases in serum ALT and AST activity in mice bearing EACs as compared to the normal group due to the induction of organ failure and metabolic disturbance caused by Ehrlich cell inoculation. These results corroborate earlier studies[61] that showed tumour mice had elevated liver enzyme levels, which are associated with cell damage, but that these markers returned to nearly normal following treatment with CAT that was shown to have a hepatoprotective effect.

3.11. Impact of CAT@CPANVs on lipid profile

Fig. 5A–C depicts the significant modulation of lipid profile parameters among the experimental groups following the administration of CAT@CPANVs treatment.

3.11.1. Impact of CAT@CPANVs on total cholesterol. Notably, total cholesterol levels exhibited significant variation among the studied groups ($F = 1919.47$, $P < 0.001$) (Fig. 5A). The EAC-bearing mice (G3) demonstrated a marked elevation in total cholesterol levels (242.35 ± 1.42 mg dL^{-1}), likely attributable to tumor-induced dyslipidemia and hepatic dysfunction. In contrast, the therapeutic administration of CAT@CPANVs (G4) resulted in a reduction of cholesterol levels to 139 ± 1.72 mg dL^{-1}, representing a substantial 42.6% decrease compared to the EAC group. This cholesterol-lowering effect was even more pronounced in the drug-only group (G2), which exhibited the lowest levels (101.43 ± 0.36 mg dL^{-1}), lower than the normal control (G1: 107.66 ± 1.84 mg dL^{-1}), suggesting a potential preventive lipid-regulating capability of CAT@CPANVs in healthy systems. The cholesterol increases in the G3 group amounted to a 115% rise relative to G1, underscoring the significant metabolic disturbance caused by EAC, while G4 effectively mitigated this rise to only 28.9% above normal.

3.11.2. Impact of CAT@CPANVs on triglyceride levels. The triglyceride levels exhibited a consistent trend across the groups studied ($F = 58.72$, $P < 0.001$) (Fig. 5A). G3 demonstrated the highest triglyceride concentration at 231.87 ± 8.81 mg dL^{-1}, aligning with the concept of metabolic reprogramming in cancer. Treatment with CAT@CPANVs in G4 significantly reduced triglyceride levels to 160.44 ± 1.75 mg dL^{-1}, representing a 30.8% decrease. In contrast, G2 recorded a level of 156.31 ± 0.79 mg dL^{-1}, which is comparable to the normal control group (G1: 148.91 ± 0.93 mg dL^{-1}). The therapeutic group thus exhibited only a 7.5% increase compared to the controls, as opposed to a 55% increase obseCated in the positive EAC group, indicating a substantial normalization of lipid metabolism following treatment.

3.11.3. Impact of CAT@CPANVs on HDL level. Importantly, the levels of high-density lipoprotein (HDL) "good cholesterol" were significantly elevated in the treated groups ($F = 134.45$, $P < 0.001$) (Fig. 5B). G4 exhibited the highest HDL levels (67.95 ± 3.01 mg dL^{-1}), representing a substantial 38.3% improvement over the control group (G1: 49.1 ± 0.83 mg dL^{-1}) and a remarkable 152% increase compared to the EAC group (G3: 26.93 ± 0.53 mg dL^{-1}). G2 also demonstrated elevated HDL level (63.85 ± 0.99 mg dL^{-1}), suggesting that CAT@CPANVs can enhance cardioprotective lipid fractions in addition to mitigating tumor-associated dyslipidemia.[62]

3.11.4. Impact of CAT@CPANVs on VLDL level. For very-low-density lipoprotein (VLDL), which is associated with triglyceride transport and often elevated in hepatic stress or cancer, there are noteworthy differences between the groups under study ($F = 59.08$, $P < 0.001$). The positive group (G3) displayed the elevated mean value (46.1 ± 1.74 mg dL^{-1}) followed by therapeutic group (G4) (32.2 ± 0.17 mg dL^{-1}), while drug group (G2) (31.11 ± 0.31 mg dL^{-1}). The control group (G1) group had lowest value (29.66 ± 0.21 mg dL^{-1}). The percentage change was higher in G2 group with 4.53%, EAC group with 55.14%, and G4 group with 8.08% when compared to G1 group (Fig. 5B). This suggests effective suppression of tumor-induced hepatic lipogenesis by CAT@CPANVs.

3.11.5. Impact of CAT@CPANVs on LDL level. The level of low-density lipoprotein (LDL), a critical indicator of atherogenic and inflammatory potential, exhibited significant differences among the groups ($P < 0.001$) (Fig. 5B). The EAC group (G3) demonstrated the highest LDL value (163.3 ± 2.95 mg dL^{-1}), indicating substantial lipid derangement attributable to tumor burden. Treatment with CAT@CPANVs in G4 resulted in a significant reduction of LDL to 40.2 ± 6.4 mg dL^{-1}, representing a 75.4% decrease compared to G3. In contrast, G2 and G1 maintained low LDL levels at 14.5 ± 0.67 and 23.2 ± 1.95 mg dL^{-1}, respectively.

These results show that CAT@CPANVs have a strong anticancer effect and significantly restore lipid homeostasis in mice with EAC. The potential of this nanoplatform in cancer treatment and prevention of metabolic consequences is highlighted by its dual control of tumor development and lipid dysregulation. Notably, these results are consistent with a prior study,[59] which shows that the serum levels of HDL, VLDL, LDL, cholesterol, and triglycerides in the EACs group of mice are significantly higher than those in the control group and lower after treatment. In the current study, tumor-bearing mice had higher serum levels of VLDL, LDL, triglycerides, and cholesterol than mice that received therapeutic treatment. The tumour cells' high energy consumption may be the cause of the elevated serum levels of these lipid indicators in the tumor-bearing animals. As a consequence, these cells improve the process of lipolysis from adipose tissues and other organs, such as the spleen and liver, increasing the majority of the serum lipid profile, while the weights of the liver and spleen have significantly decreased, there has also been a highly substantial decrease in the overall amount of lipid in the liver tissue.[63]

3.12. Antioxidants activity of CAT@CPANVs

In cancer care, oxidative stress plays a crucial role in tumour growth, maintenance, and prevention. Because tumor cells actively create oxygen and lack proper oxidation–reduction control, oxidative stress occurs in tumor-bearing conditions.[64] Oxidative stress is a causal factor in the toxicology of major therapeutic chemotherapies.[65] Oxidative stress was shown by elevated malondialdehyde (MDA), a lipid peroxidation byproduct. GSH, CAT, and SOD are key antioxidant system effectors that scavenge reactive oxygen species (ROS) to protect cells.[64] Results show that the positive group had higher malondialdehyde (MDA) levels and lower antioxidant protein compared to controls.[66]

3.12.1. Impact of CAT@CPANVs on GSH level in liver tissue. Details for GSH activity (mg g^{-1} tissue) were given, as seen in Fig. 5C. The GSH activity values in the EACs groups are significantly lower ($p < 0.001$) than in the drug and negative control groups. In terms of GSH activity, the therapeutic group has a much higher level than the EACs group. The GSH level in liver tissue varies significantly between the groups under

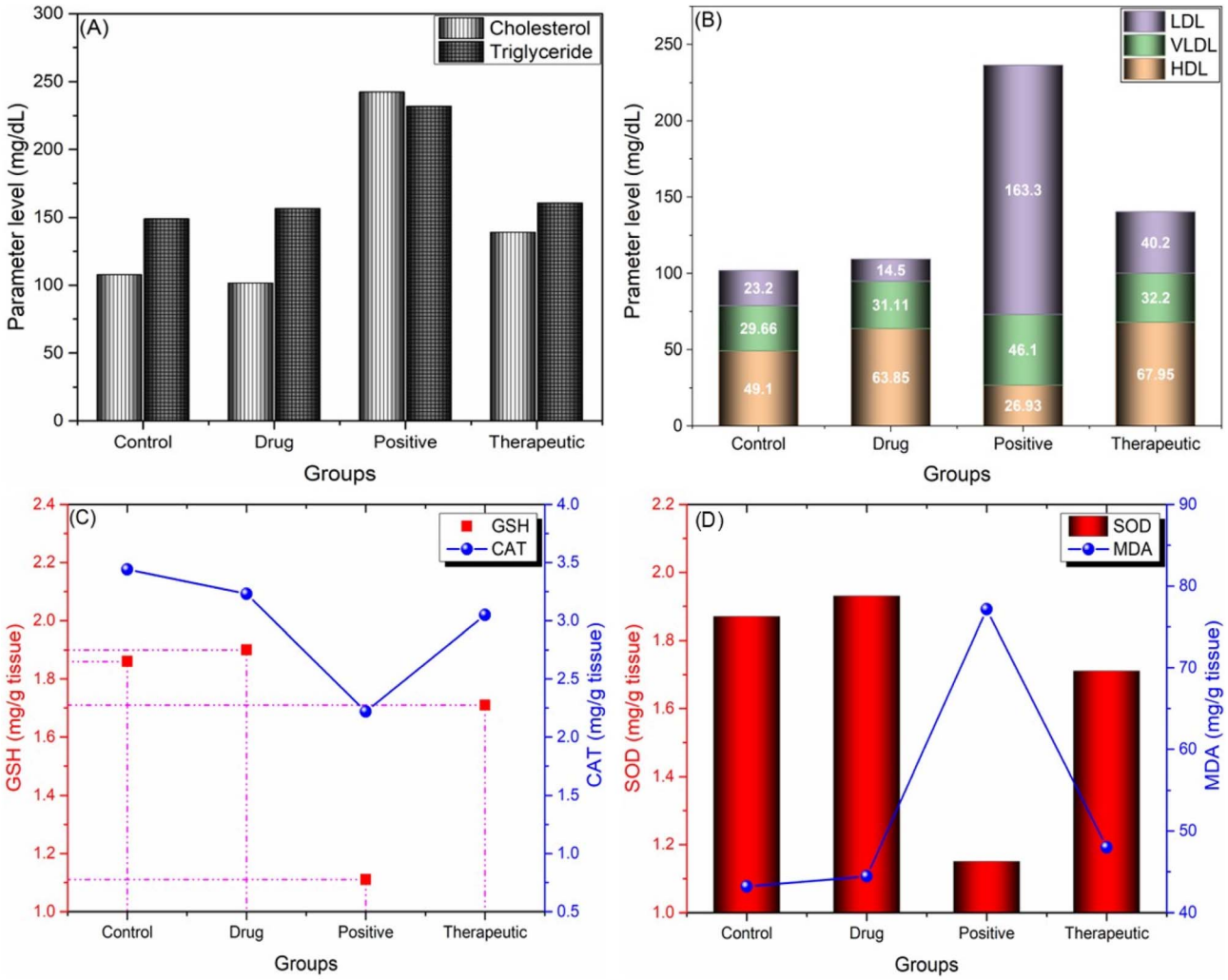

Fig. 5 Therapeutic impacts of the CAT@CPANVs on the levels of: (A) cholesterol and triglyceride, (B) HDL and VLDL, LDL, (C) GSH and Cat, (D) SOD and MDA (mg g^{-1} tissue). G1 (control) was given 10 days of intraperitoneal injection (IPJ) of normal saline; G2 (drug group) received IP administration of CAT@CPANVs (15 mg kg^{-1}) daily for 10 days. G3 (EAC-positive group) was administered EACs (2.5 $\times 10^6$ cells per mice) by IPJ on the initial day; G4 (therapeutic group) CAT@CPANVs were given IP at 15 mg kg^{-1} daily for 10 days after EAC injection.

investigation ($F = 5.71$, $P < 0.001$). The control groups (G1) had the highest mean value (3.44 ± 0.16), followed by the drug group (G2) (3.23 ± 0.17) and the therapeutic group (G4) (3.05 ± 0.17). Positive group (G3) had lowest value (2.22 ± 0.42). As compared to the control, the drug control showed a substantial drop in percentage change (−5.61%), followed by the positive group (−34.30%) and the therapeutic group (−8.98%).

3.12.2. Impact of CAT@CPANVs on the catalase activity in liver tissues. The catalase activity data (in mg g^{-1} tissue) are shown, as illustrated in Fig. 5C. When the EACs groups are compared to the drug and negative control groups, their catalase activity values are significantly reduced ($p < 0.001$). As far as catalase activity is concerned, the therapeutic group significantly outperforms the EACs group. The degree of Catalase activity in liver tissue varies significantly between the groups under investigation ($F = 136.23$, $P < 0.001$). The drug groups (G2) had the highest mean value (1.9 ± 0.02), followed by control group (G1) (1.86 ± 0.01) and (G4) group (1.71 ± 0.01), (G3) EAC group had lowest value (1.11 ± 0.04). Only drug group had a rise in percentage change (2.51%), whereas the positive control saw a significant decline (−38.82%), and the treatment group saw a significant decrease (−7.85%) when compared to the negative control.

3.12.3. Impact of CAT@CPANVs on SOD in liver tissues. The information for SOD activity (mg g^{-1} tissue) is given, as seen in Fig. 5D. In comparison to drug and control groups, the EACs groups exhibit significantly decreased SOD activity values ($p < 0.001$). Regarding SOD activity, the treatment group exhibits a significant increase in comparison to the EACs group. The SOD level in liver tissue varied significantly between the groups under investigation, according to the liver results ($F = 136.23$, $P < 0.001$). The drug group (G2) had the highest mean value (1.93 ± 0.04) then (G1) group (1.87 ± 0.02) and (G4) group (1.71 ± 0.03), the EAC (G3) group had the smallest amount (1.15 ± 0.05). When comparing the percentage change to the control group, the drug group showed the only rise (2.51%), while the

positive control showed a substantial reduction (−38.82%), and the therapeutic group showed a significant decline (−7.85%).

3.12.4. Impact of CAT@CPANVs on malondialdehyde (MDA) in liver tissue. The results regarding MDA values (in mg g^{-1} tissue) are given, as Fig. 5D illustrates. The MDA readings in the EACs groups are significantly greater ($p < 0.001$) than in G2 and G1 groups. In terms of MDA values, G4 group exhibits lower significance than the EACs G3 group. The MDA level in liver tissue varied significantly between the groups under investigation, according to the liver results ($F = 30.69$, $P < 0.001$). In the positive group, the high mean value was noted (G3) (77.15 ± 3.72) followed by therapeutic group (G4) (48.01 ± 1.95) while the drug group (G2) (44.45 ± 2.32) and control group (G1) had lowest value (43.2 ± 231). With respect to the negative control, the percentage change was lower in drug group (−0.27%), higher in the therapeutic group (6.35%) and higher in the positive group (72.54%). The present findings corroborate previous research,[67] which identified reduced levels of GSH, CAT, and SOD activity, alongside elevated MDA levels in EAC-bearing mice. This is consistent with earlier studies[68] that reported diminished CAT and SOD activity and increased MDA levels in EAC-bearing mice. Additionally, prior investigations[59,61] have demonstrated that mice with EAC exhibit higher MDA levels and reduced GSH and SOD activity. The recent study suggests that CAT@CPANVs can improve liver function by increased values of SOD, GSH, CAT, and decrease of MDA. CAT@CPANVs have the potential to prevent liver damage. This study indicates that CAT@CPANVs can enhance liver function by elevating the levels of GSH, CAT, and SOD, while decreasing levels of MDA. CAT@CPANVs have the potential to prevent liver injury. Moreover, the present study revealed a significant decrease in GSH levels in the blood of tumor-bearing mice. Reduced glutathione is vital to the body's antioxidant defences since it is an important cofactor for antioxidant enzymes.[69] Lipid peroxidation is elevated due to the depletion of GSH reseCates, which normally have the ability to moderate the amount of lipid peroxidation. The glutathione-related enzymes employ glutathione during oxidative stress to detoxify peroxides that are created due to elevated lipid peroxidation.[70] Low MDA levels imply that there is inhibition of lipid peroxidation.[71] As a result, there was less MDA visible after treatment with CAT@CPANVs, which prevented cellular damage. Cells need both enzymatic and non-enzymatic antioxidants to get rid of free radicals. It has been proposed that the deficiencies in activities of SOD, CAT, and GSH in tumor-bearing mice may be due to activity decreased in the mitochondria. The current study suggests that CAT@CPANVs may increase GSH levels.

3.12.5. Impact of CAT@CPANVs on caspase 3 and Bcl2 in liver tissue. Levels of caspase 3 and Bcl2 in EAC G3 group were greater in the recent work when compared to G1 and G2 groups (Fig. 6). The findings align with those of a different research discovered that in comparison to the normal control group, EAC inoculation resulted in a large increase in hepatic caspase 3 and a considerable decrease in hepatic Bcl2 levels.[72] Given recent results, Badr El-Din *et al.*[73] reported that mice inoculated with Ehrlich ascites carcinoma showed notable differences in the expression of apoptotic regulators (activation of caspase-3,

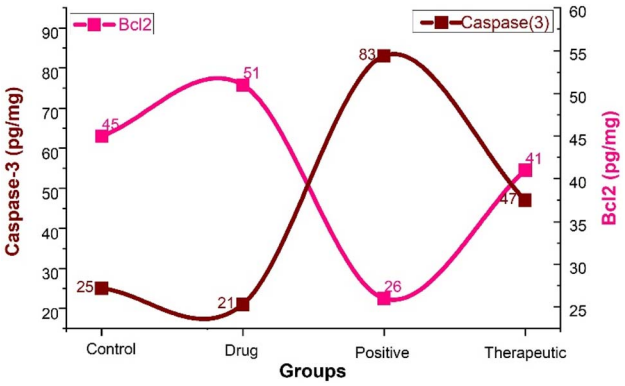

Fig. 6 Effects of different treatments on the levels of caspase 3 (Pg mg^{-1} tissue) and Bcl2 (ng mg^{-1} tissue) in all tested groups.

upregulation of proapoptotic proteins Bax and p53, downregulation of the antiapoptotic protein Bcl-2, and decreased Bcl2: Bax ratio). The therapeutic group's elevated Bcl2 and decreased caspase 3 levels suggested a reduction in liver apoptosis.

3.13. Immunohistochemical analysis

Immunohistochemical analyses demonstrated that liver tissue slices from the negative control group had considerably moderate levels of TNF-α immunoreactivity (Fig. 7A), but the drug group's liver tissue only had mild expression of TNF-α (Fig. 7B). Comparing liver sections from the positive EACs control group to those from the control group, the former displayed noticeably greater levels of TNF-α immunoreactivity in the liver tissue (Fig. 7C). In contrast to the control group, liver slices from the therapeutic group of mice displayed nearly mild levels of TNF-α immunoreactivity (Fig. 7D).

According to Yoo *et al.*[74] and Ankoma-Sey *et al.*,[75] cancer cells stimulate angiogenesis by secreting more angiogenic growth factors like TNF-α, VEGF, PIGF, and TGF-β in addition to other cytokines. Because of these recently developed capillaries, angiogenic factors and cytokines that have already been produced enter the portal vein and circulatory system, eventually arriving in the liver where they bind to particular receptors to trigger a variety of signal transductions. The characteristics of hepatic inflammation and fibrosis are mediated by hepatic stellate cells, Kupffer cells, and mast cells, and ultimately, liver injury are further activated as a result of this pathological occurrence.[76] On the other hand, other chemokines that are expressed when these hepatic stellate cells are activated are also in charge of stimulating angiogenesis, inflammation, and fibrosis.[77] Compared to the G1 group, the G3 group's mice's liver slices displayed noticeably more TNF-α immunoreactivity in the liver tissue. However, a slightly higher amount of TNF-α was found in liver sections from mice in the treatment group compared to the control group, suggesting a reduction in liver inflammation.

3.14. Impact of CAT@CPANVs on liver histology

Microscopic image of liver sections in the control group (G1) demonstrating a typical configuration of hepatic cords with

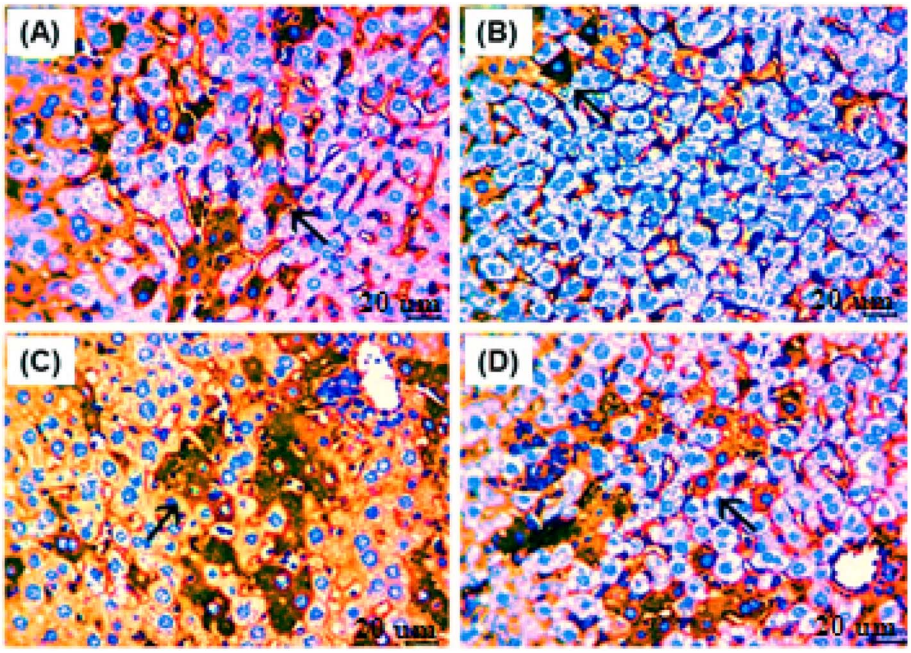

Fig. 7 Under a microscope, TNF-α expression in liver sections can be seen as follows: (A) the control group with moderate TNF-α cytoplasmic staining reaction; (B) the drug group with mild TNF-α cytoplasmic staining reaction in the hepatic tissue; (C) the EACs positive group with strong TNF-α cytoplasmic staining reactivity in the hepatic tissue; and (D) the therapeutic group with nearly mild TNF-α cytoplasmic staining reaction in the liver tissue. 20 μm is the scale bar.

normal portal regions, sinusoids, and central vein as displayed in (Fig. 8A). The drug group (G2)'s liver sections exhibit improved hepatic tissue histology and decreased cellular filtrates (black arrow heads), as seen in (Fig. 8B). As seen in (Fig. 8C), liver sections from the EAC group (G3) displayed multifocal areas of hepatocytes coagulative necrosis (black arrows), portal fibrosis (blue arrows), and inflammation (yellow arrows), along with enormous EAC cell aggregation mixed to mononuclear cells in portal areas (black arrow heads). The histology of the hepatic tissue has improved in the liver sections of therapeutic group (G4), as seen in (Fig. 8D).

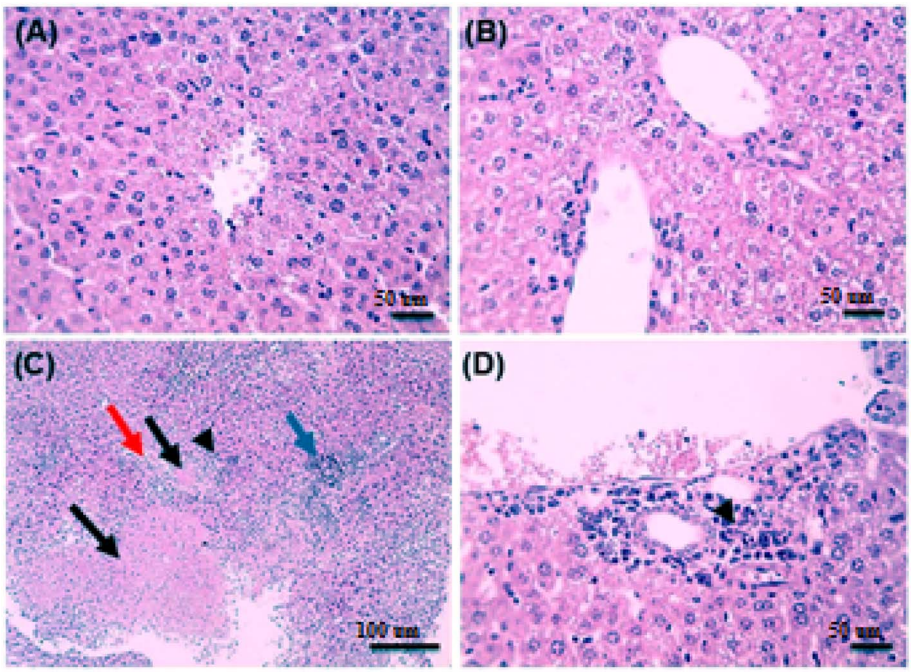

Fig. 8 The following are the magnification levels for an image of the liver histology under a microscope in (A) the G1 tissue, (B) the G2 tissue, (C) the G3 EAC tissue, and (D) the G4 tissue: both high (X:400 bar 50) and low (X:100 bar 100).

4. Conclusion

This study demonstrated how CAT@CPANVs offers a workable platform for application in the medical field. The CAT@CPANVs nanoformulation was created by encapsulating CAT with CPANVs. Strong H-bonding interactions between the OH groups of the phenolic compounds' chitosan chain and the lipid matrix were responsible for the nanoformulation's exceptional physiologic stability. Furthermore, CPANVs demonstrated a high percentage of CAT loading content, encapsulation effectiveness, and pH-dependent CAT release properties. The *in vivo* trial shows that this unique technique provides an affordable way to preseCate the medicine after it is encapsulated by CPANVs, allowing for a more targeted and extended release of the drug, lowering the volume and count of EAC, and enhancing liver functions. Lipid profile can be enhanced by CAT@CPANVs. Based on biochemical, immunohistochemical, and histological studies, the special CAT@CPANVs agent improved liver tissues without causing any discernible side effects. Histology shows that the liver tissue that was treated with CAT-QCNP is now better. The histopathology of the liver tissue treated with CAT@CPANVs demonstrates improvement. This can be achieved by decreasing apoptosis and recovering antioxidant properties, which eradicate oxidative stress and maintain the health of the liver's blood vessels.

Ethical statement

In compliance with the National Institutes of Health's (NIH) guidelines for the care and use of laboratory animals [5], Suez University's Institutional Animal Ethics Committee (IAEC) approved all experimental methods (Approval No. SUEZ Sci_IRB:19/04/2025/22).

Author contributions

M. Y. A.: software, validation, visualization, writing – original draft, writing – review & editing. M. R. A.: software, validation, visualization, writing – original draft, writing – review & editing. W. A. E.: data curation, software, validation, visualization, writing – original draft. A. A. S.: software, validation, visualization, writing – original draft, writing – review & editing. S. I. E.: data curation, methodology, software, validation, writing – original draft. R. F. M.: conceptualization, data curation, methodology, validation, visualization, writing – original draft, writing – review & editing. W. M. S.: data curation, methodology, validation, visualization, writing – original draft, writing – review & editing. Y. A. H.: software, validation, visualization, writing – original draft, writing – review & editing.

Conflicts of interest

The authors declare no conflict of interest.

Data availability

The raw data supporting the conclusions of this article will be made available by the authors upon request.

Supplementary information is available. See DOI: https://doi.org/10.1039/d5ra06086a.

Acknowledgements

The authors extend their appreciation to the University Higher Education Fund for funding this research work under Research Support Program for Central labs at King Khalid University through the Project number (CL/CO/B/3) for funding this research work.

References

1 D. R. Radulski, M. C. Stipp, C. M. Galindo and A. Acco, Features and applications of Ehrlich tumor model in cancer studies: a literature review, *Transl. Breast Cancer Res.*, 2023, **30**(4), 22.
2 S. Yılmaz, A. Tokpınar, E. Eroğlu, Ş. Ateş, R. Zahid, S. Avnioğlu, Ö. Bozkurt and M. Nisari, The effect of antioxidants in Ehrlich Ascites Cancer, *Cell. Mol. Biol.*, 2021, **67**(2), 20–24.
3 A. Baranwal, P. Aggarwal, A. Rai and N. Kumar, Pharmacological actions and underlying mechanisms of catechin: A review, *Mini-Rev. Med. Chem.*, 2022, **22**(5), 821–833.
4 A. Ganeshpurkar and A. Saluja, The pharmacological potential of catechin, *Indian J. Biochem. Biophys.*, 2020, **57**(5), 505–511.
5 D. Shikha, A. Singh, N. K. Rangra, V. Monga and R. Bhatia, Insights to therapeutic potentials, pharmaceutical formulations, chemistry and analytical methods of catechin, *Phytochem. Rev.*, 2024, **23**(5), 1557–1598.
6 A. N. Dos Santos, T. R. de L Nascimento, B. L. Gondim, M. M. Velo, R. I. de A. Rêgo, J. R. do C. Neto, J. R. Machado, M. V. da Silva, H. W. de Araújo, M. G. Fonseca and L. R. Castellano, Catechins as model bioactive compounds for biomedical applications, *Curr. Pharm. Des.*, 2020, **26**(33), 4032–4047.
7 M. Alavi, R. Yarani, M. Sreedharan and S. Thomas, Micro and nanoformulations of catechins for therapeutic applications: recent advances and challenges, *Micro Nano Bio Aspects*, 2023, **2**(1), 8–19.
8 E. Garbayo, S. Pascual-Gil, C. Rodríguez-Nogales, L. Saludas, A. Estella-Hermoso de Mendoza and M. J. Blanco-Prieto, Nanomedicine and drug delivery systems in cancer and regenerative medicine, *Wiley Interdiscip. Rev.: Nanomed. Nanobiotechnology*, 2020, **12**(5), e1637.
9 M. Piatkowski, J. Radwan-Pragłowska and K. Raclavský, Application of Poly (aspartic acid) and its Derivatives in Medicine and Pharmacy, *Asian J. Appl. Sci.*, 2015, **3**(5), 718–723.
10 A. Stefanache, I. I. Lungu, N. Anton, D. Damir, C. Gutu, I. Olaru, A. Plesea Condratovici, M. Duceac, M. Constantin

and G. Calin, Chitosan Nanoparticle-Based Drug Delivery Systems: Advances, Challenges, and Future Perspectives, *Polymers*, 2025, **17**(11), 1453.

11 D.-Y. Zhang, X.-Z. Shen, J.-Y. Wang, L. Dong, Y.-L. Zheng and L.-L. Wu, Preparation of chitosan-polyaspartic acid-5-fluorouracil nanoparticles and its anti-carcinoma effect on tumor growth in nude mice, *World J. Gastroenterol.*, 2008, **14**(22), 3554.

12 C. L. Zegarra-Urquia, J. Santiago, J. D. Bumgardner, J. Vega-Baudrit, C. A. Hernández-Escobar and E. A. Zaragoza-Contreras, Synthesis of nanoparticles of the chitosan-poly ((α, β)-DL-aspartic acid) polyelectrolite complex as hydrophilic drug carrier, *Int. J. Polym. Mater. Polym. Biomater.*, 2023, **72**(6), 497–506.

13 X. Jiao, X. Chong, H. Du, M. Yang, Z. Zhu, Z. Ma and Y. Wen, Development of pH and enzyme dual responsive chitosan/polyaspartic acid nanoparticle-embedded nanofibers for fruit preservation, *Int. J. Biol. Macromol.*, 2025, **297**, 139903.

14 D. W. Tang, S. H. Yu, Y. C. Ho, B. Q. Huang, G. J. Tsai, H. Y. Hsieh, H. W. Sung and F. L. Mi, Characterization of tea catechins-loaded nanoparticles prepared from chitosan and an edible polypeptide, *Food Hydrocolloids*, 2013, **30**(1), 33–41.

15 D. B. Mondal, J. M. Velayudhan, A. Lekshman, R. S. K. Mandal, R. Raja and N. Kumar, in *Tissue Scaffolds*, ed. N. Kumar, V. Kumar, S. Shrivastava, A. K. Gangwar and S. Saxena, Springer US, New York, NY, 2022, DOI: DOI: 10.1007/978-1-0716-2425-8_31, pp. 399–422.

16 Y. Liu, Y. Fan, L. Gao, Y. Zhang and J. Yi, Enhanced pH and thermal stability, solubility and antioxidant activity of resveratrol by nanocomplexation with α-lactalbumin, *Food Funct.*, 2018, **9**(9), 4781–4790.

17 M. Barzegar-Jalali, Kinetic analysis of drug release from nanoparticles, *J. Pharm. Pharm. Sci.*, 2008, **11**(1), 167–177.

18 B. T. Doumas, W. A. Watson and H. G. Biggs, Albumin standards and the measurement of serum albumin with bromocresol green, *Clin. Chim. Acta*, 1971, **31**(1), 87–96.

19 A. G. Gornall, C. J. Bardawill and M. M. David, Determination of serum proteins by means of the biuret reaction, *J. Biol. Chem.*, 1949, **177**(2), 751–766.

20 S. Reitman and S. Frankel, A colorimetric method for the determination of serum glutamic oxalacetic and glutamic pyruvic transaminases, *Am. J. Clin. Pathol.*, 1957, **28**(1), 56–63.

21 C. C. Allain, L. S. Poon, C. S. Chan, W. F. Richmond and P. C. Fu, Enzymatic determination of total serum cholesterol, *Clin. Chem.:Princ. Tech., 2nd Ed.*, 1974, **20**(4), 470–475.

22 H. Wieland and D. Seidel, A simple specific method for precipitation of low density lipoproteins, *J. Lipid Res*, 1983, **24**(7), 904–909.

23 P. Fossati and L. Prencipe, Serum triglycerides determined colorimetrically with an enzyme that produces hydrogen peroxide, *Clin. Chem.:Princ. Tech., 2nd Ed.*, 1982, **28**(10), 2077–2080.

24 C. A. Albert and A. Funso, Oxidative stress and oxidative damage in male rat erythrocytes associated with prolonged exposure to smoke pollution, *J. Environ. Prot.*, 2012, **2012**, 414–419.

25 H. Aebi, Catalase in vitro, *Methods Enzymol.*, 1984, **105**, 121–126.

26 M. Nishikimi, N. A. Rao and K. Yagi, The occurrence of superoxide anion in the reaction of reduced phenazine methosulfate and molecular oxygen, *Biochem. Biophys. Res. Commun.*, 1972, **46**(2), 849–854.

27 S. Kei, Serum lipid peroxide in cerebrovascular disorders determined by a new colorimetric method, *Clin. Chim. Acta*, 1978, **90**(1), 37–43.

28 K. S. Suvarna, C. Layton and J. D. Bancroft, *Bancroft's Theory and Practice of Histological Techniques E-Book*, Elsevier health sciences, 2018.

29 J. Alkabli, M. A. Rizk, R. F. M. Elshaarawy and W. N. El-Sayed, Ionic chitosan Schiff bases supported Pd (II) and Ru (II) complexes; production, characterization, and catalytic performance in Suzuki cross-coupling reactions, *Int. J. Biol. Macromol.*, 2021, **184**, 454–462.

30 J. Chen, L. Xu, J. Han, M. Su and Q. Wu, Synthesis of modified polyaspartic acid and evaluation of its scale inhibition and dispersion capacity, *Desalination*, 2015, **358**, 42–48.

31 D. Kołodyńska, Chitosan as an effective low-cost sorbent of heavy metal complexes with the polyaspartic acid, *Chem. Eng. J.*, 2011, **173**(2), 520–529.

32 Y. Zheng, W. Yang, C. Wang, J. Hu, S. Fu, L. Dong, L. Wu and X. Shen, Nanoparticles based on the complex of chitosan and polyaspartic acid sodium salt: preparation, characterization and the use for 5-fluorouracil delivery, *Eur. J. Pharm. Biopharm.*, 2007, **67**(3), 621–631.

33 B. Liu, Y. Wang, Q. Yu, D. Li and F. Li, Synthesis, characterization of catechin-loaded folate-conjugated chitosan nanoparticles and their anti-proliferative effect, *J. Food*, 2018, **16**(1), 868–876.

34 W. Abd El-Fattah, A. Guesmi, N. B. Hamadi, M. R. Abdulbaqi, A. Shahat, R. F. M. Elshaarawy and Y. A. Hassan, Encapsulation of Plicosepalus curviflorus-derived polyphenols in chitosan-alginate microvehicles for potent anticancer uses: Optimization using response surface methodology, *Int. J. Biol. Macromol.*, 2025, 145741.

35 G. Midekessa, K. Godakumara, J. Ord, J. Viil, F. Lättekivi, K. Dissanayake, S. Kopanchuk, A. Rinken, A. Andronowska and S. Bhattacharjee, Zeta potential of extracellular vesicles: toward understanding the attributes that determine colloidal stability, *ACS Omega*, 2020, **5**(27), 16701–16710.

36 H. W. Alhamdi, N. F. Alqahtani, E. Fayad, L. A. Salama, H. A. Katouah, D. S. Alshaya, M. Y. Alfaifi, S. E. I. Elbehairi, A. A. Elkashef and R. F. M. Elshaarawy, Synthesis, characterization, and pharmaceutical activities of new metallated ionic chitosan Schiff base hydrogels as potential chemotherapeutic agents, *React. Funct. Polym.*, 2025, **212**, 106212.

37 H. W. Alhamdi, E. Fayad, M. Y. Alfaifi, H. A. Katouah, D. S. Alshaya, A. A. Shati, S. E. I. Elbehairi, R. F. M. Elshaarawy and W. M. Serag, Chitosan-Ascorbate

Nanocapsules for Sustained Cisplatin Release: Minimizing Nephrotoxicity via Anti-Inflammatory and Anti-Apoptotic Mechanisms, *J. Drug Delivery Sci. Technol.*, 2025, 106968.

38 F. Li, H. Jin, J. Xiao, X. Yin, X. Liu, D. Li and Q. Huang, The simultaneous loading of catechin and quercetin on chitosan-based nanoparticles as effective antioxidant and antibacterial agent, *Food Res. Int.*, 2018, **111**, 351–360.

39 Y. Zi, K. Yang, J. He, Z. Wu, J. Liu and W. Zhang, Strategies to enhance drug delivery to solid tumors by harnessing the EPR effects and alternative targeting mechanisms, *Adv. Drug Delivery Rev.*, 2022, **188**, 114449.

40 S. R. Falsafi, H. Rostamabadi, E. Assadpour and S. M. Jafari, Morphology and microstructural analysis of bioactive-loaded micro/nanocarriers via microscopy techniques; CLSM/SEM/TEM/AFM, *Adv. Colloid Interface Sci.*, 2020, **280**, 102166.

41 K. Khodaverdi, A. Bakhshi, M. R. Mozafari and S. M. Naghib, A review of chitosan-based nanocarriers as drug delivery systems for brain diseases: Critical challenges, outlooks and promises, *Int. J. Biol. Macromol.*, 2024, **278**, 134962.

42 A. M. Nasr, S. M. Aboelenin, M. Y. Alfaifi, A. A. Shati, S. E. I. Elbehairi, R. F. M. Elshaarawy and N. H. A. Elwahab, Quaternized chitosan thiol hydrogel-thickened nanoemulsion: A multifunctional platform for upgrading the topical applications of virgin olive oil, *Pharmaceutics*, 2022, **14**(7), 1319.

43 Z. H. Chen, C. Kim, X.-b. Zeng, S. H. Hwang, J. Jang and G. Ungar, Characterizing size and porosity of hollow nanoparticles: SAXS, SANS, TEM, DLS, and adsorption isotherms compared, *Langmuir*, 2012, **28**(43), 15350–15361.

44 H. Jeong, K. J. Samdani, D. H. Yoo, D. W. Lee, N. H. Kim, I.-S. Yoo and J. H. Lee, Resveratrol cross-linked chitosan loaded with phospholipid for controlled release and antioxidant activity, *Int. J. Biol. Macromol.*, 2016, **93**, 757–766.

45 J. Wu, Y. Wang, H. Yang, X. Liu and Z. Lu, Preparation and biological activity studies of resveratrol loaded ionically cross-linked chitosan-TPP nanoparticles, *Carbohydr. Polym.*, 2017, **175**, 170–177.

46 W. Xiong, C. Ren, J. Li and B. Li, Enhancing the photostability and bioaccessibility of resveratrol using ovalbumin–carboxymethylcellulose nanocomplexes and nanoparticles, *Food Funct.*, 2018, **9**(7), 3788–3797.

47 Q. E. Jin, H. Chen, A. Luo, F. Ding and Z. Liu, S100A14 stimulates cell proliferation and induces cell apoptosis at different concentrations via receptor for advanced glycation end products (RAGE), *PloS One*, 2011, **6**(4), e19375.

48 W. M. Serag and B. E. Elsayed, Detection of liver fibrosis stages in patients with hepatitis C virus infection by non-invasive tool, *Egypt. Liver J.*, 2021, **11**(1), 9.

49 D. Sapkota, D. E. Costea, M. Blø, O. Bruland, J. B. Lorens, E. N. Vasstrand and S. O. Ibrahim, S100A14 inhibits proliferation of oral carcinoma derived cells through G1-arrest, *Oral Oncol.*, 2012, **48**(3), 219–225.

50 A. R. Bresnick, D. J. Weber and D. B. Zimmer, S100 proteins in cancer, *Nat. Rev. Cancer*, 2015, **15**(2), 96–109.

51 C. Xu, H. Chen, X. Wang, J. Gao, Y. Che, Y. Li, F. Ding, A. Luo, S. Zhang and Z. J. Liu, a member of the EF-hand calcium-binding proteins, is overexpressed in breast cancer and acts as a modulator of HER2 signaling, *J. Biol. Chem.*, 2014, **289**(2), 827–837.

52 M. Tabata, T. Kadomatsu, S. Fukuhara, K. Miyata, Y. Ito, M. Endo, T. Urano, H. J. Zhu, H. Tsukano and H. Tazume, Angiopoietin-like protein 2 promotes chronic adipose tissue inflammation and obesity-related systemic insulin resistance, *Cell Metab.*, 2009, **10**(3), 178–188.

53 J. K. Dowman, J. W. Tomlinson and P. N. Newsome, Systematic review: the diagnosis and staging of non-alcoholic fatty liver disease and non-alcoholic steatohepatitis, *Aliment. Pharmacol. Ther.*, 2011, **33**(5), 525–540.

54 Z. Tian, K. Miyata, T. Kadomatsu, H. Horiguchi, H. Fukushima, S. Tohyama, Y. Ujihara, T. Okumura, S. Yamaguchi and J. Zhao, ANGPTL2 activity in cardiac pathologies accelerates heart failure by perturbing cardiac function and energy metabolism, *Nat. Commun.*, 2016, **7**(1), 13016.

55 Y. Toiyama, K. Tanaka, T. Kitajima, T. Shimura, H. Imaoka, K. Mori, M. Okigami, H. Yasuda, Y. Okugawa, S. Saigusa and M. Ohi, Serum angiopoietin-like protein 2 as a potential biomarker for diagnosis, early recurrence and prognosis in gastric cancer patients, *Carcinogenesis*, 2015, **36**(12), 1474–1483.

56 N. G. Gowda, V. D. Shiragannavar, S. C. Prabhuswamimath, S. Tuladhar, S. B. Chidambaram and P. K. Santhekadur, Ehrlich Ascites carcinoma mice model for studying liver inflammation and fibrosis, *Adv. Cancer Biol.:Metastasis*, 2022, **4**, 100029.

57 W. M. Ibrahim and S. M. Foad, Biochemical study in Ehrlich carcinoma cells-bearing mice treated with arsenic trioxide and cisplatin, *Adv. Environ. Life Sci.*, 2022, **1**(1), 40–47.

58 E. S. Kotb, H. W. Alhamdi, M. Y. Alfaifi, O. Darweesh, A. A. Shati, S. E. Elbehairi, W. M. Serag, Y. A. Hassan and R. F. Elshaarawy, Examining the quaternary ammonium chitosan Schiff base-ZnO nanocomposite's potential as protective therapy for rats' cisplatin-induced hepatotoxicity, *Int. J. Biol. Macromol.*, 2024, **276**, 133616.

59 E. S. Toson, F. M. Almutairi, A. A. Elfalal, S. A. Habib, R. F. Zahran and M. Elbakry, Suppression Effect of Superoxide Dismutase (SOD)-Like Activity Protein Partially Purified from Raphnus sativus Leaves against Liver Metastasis in Mice Intraperitoneally Infected with Ehrlich Ascites Carcinoma Cell, *Nat. Sci.*, 2016, **8**(7), 321–332.

60 G. Abu-Sinna, A. Y. Esmat, A. A. Al-Zahaby, N. A. Soliman and T. M. Ibrahim, Fractionation and characterization of Cerastes cerastes cerastes snake venom and the antitumor action of its lethal and non-lethal fractions, *Toxicon*, 2003, **42**(2), 207–215.

61 M. F. Elsadek, M. M. E. El-Din and B. M. Ahmed, Evaluation of anticarcinogenic and antioxidant properties of Eruca sativa extracts versus Ehrlich ascites carcinoma in mice, *J. King Saud Univ., Sci.*, 2021, **33**(4), 101435.

62 G. Zhu, L. Cao, J. Wu, M. Xu, Y. Zhang, M. Wu and J. Li, Co-morbid intersections of cancer and cardiovascular disease

and targets for natural drug action: Reprogramming of lipid metabolism, *Biomed. Pharmacother.*, 2024, **176**, 116875.

63 H. Korekane, A. Nishikawa and K. Imamura, Mechanisms mediating metabolic abnormalities in the livers of Ehrlich ascites tumor-bearing mice, *Arch. Biochem. Biophys.*, 2003, **412**(2), 216–222.

64 D. S. Morsi, I. O. Barnawi, H. M. Ibrahim, A. M. El-Morsy, M. A. El Hassab and H. M. HM Abd El Latif, Immunomodulatory, apoptotic and anti-proliferative potentials of sildenafil in Ehrlich ascites carcinoma murine model: In vivo and in silico insights, *Int. Immunopharmacol.*, 2023, **119**, 110135.

65 H. S. Hafez, E. S. Kotb, Z. El-Khayat, R. F. Elshaarawy and W. M. Serag, The diminution and modulation role of water-soluble gallic acid-carboxymethyl chitosan conjugates against the induced nephrotoxicity with cisplatin, *Sci. Rep.*, 2022, **12**(1), 19903.

66 A. Sofo, B. Dichio, C. Xiloyannis and A. Masia, Antioxidant defences in olive trees during drought stress: changes in activity of some antioxidant enzymes, *Funct. Plant Biol.*, 2005, **32**(1), 45–53.

67 D. Ashokkumar, U. K. Mazumder, M. Gupta and V. T. Selvan, Effect on Inhibition of Proliferation and Antioxidant Enzyme Level of Lippia nodiflora in EAC Cell Line Treated Mice, *J. Complementary Integr. Med.*, 2009, **6**(1), 1–16.

68 A. A. Mohamed, S. S. El-Kholy, N. Dahran, K. M. El Bohy, G. G. Moustafa, T. M. Saber, M. M. Metwally, R. A. Gaber, L. S. Alqahtani, G. Mostafa-Hedeab and E. S. El-Shetry, Scrutinizing pathways of nicotine effect on renal Alpha-7 nicotinic acetylcholine receptor and Mitogen-activated protein kinase (MAPK) expression in Ehrlich ascites carcinoma-bearing mice: Role of Chlorella vulgaris, *Gene*, 2022, **837**, 146697.

69 J. D. Hayes, J. U. Flanagan and I. R. Jowsey, Glutathione transferases, *Annu. Rev. Pharmacol. Toxicol.*, 2005, **45**(1), 51–88.

70 K. S. El-Gendy, N. M. Aly, F. H. Mahmoud, A. Kenawy and A. K. El-Sebae, The role of vitamin C as antioxidant in protection of oxidative stress induced by imidacloprid, *Food Chem. Toxicol.*, 2010, **48**(1), 215–221.

71 P. Chaturvedi, Inhibitory response of Raphanus sativus on lipid peroxidation in albino rats. Evidence-Based Complementary and Alternative, *Medicine*, 2008, **5**(1), 55–59.

72 E. H. Abu-Zeid, E. W. El-Hady, G. A. Ahmed, Y. M. Abd-Elhakim, D. Ibrahim, N. A. Abd-Allah, A. H. Arisha, M. S. Sobh and A. M. A. Abo-Elmaaty, Nicotine exacerbates liver damage in a mice model of Ehrlich ascites carcinoma through shifting SOD/NF-κB/caspase-3 pathways: Ameliorating role of Chlorella vulgaris, *Naunyn-Schmiedeberg's Arch. Pharmacol.*, 2024, **397**(10), 7767–7783.

73 N. K. B. El-Din, D. A. Ali and R. F. Abou-El-Magd, Grape seeds and skin induce tumor growth inhibition via G1-phase arrest and apoptosis in mice inoculated with Ehrlich ascites carcinoma, *Nutrition*, 2019, **58**, 100–109.

74 B. K. Yoo, L. Emdad, S. G. Lee, Z. Z. Su, P. Santhekadur, D. Chen, R. Gredler, P. B. Fisher and D. Sarkar, Astrocyte elevated gene-1 (AEG-1): A multifunctional regulator of normal and abnormal physiology, *Pharmacol. Ther.*, 2011, **130**(1), 1–8.

75 V. Ankoma-Sey, Y. Wang and Z. Dai, Hypoxic stimulation of vascular endothelial growth factor expression in activated rat hepatic stellate cells, *Hepatology*, 2000, **31**(1), 141–148.

76 P. K. Santhekadur, M. Akiel, L. Emdad, R. Gredler, J. Srivastava, D. Rajasekaran, C. L. Robertson, N. D. Mukhopadhyay, P. B. Fisher and D. Sarkar, Staphylococcal nuclease domain containing-1 (SND1) promotes migration and invasion via angiotensin II type 1 receptor (AT1R) and TGFβ signaling, *FEBS Open Bio*, 2014, **4**, 353–361.

77 R. Ma, Y. Feng, S. Lin, J. Chen, H. Lin, X. Liang, H. Zheng and X. Cai, Mechanisms involved in breast cancer liver metastasis, *J. Transl. Med.*, 2015, **13**(1), 64.